Effect of topological disorder on structural, mechanical, and electronic properties of amorphous silicon nitride: An atomistic study

Ravi Pramod Vedula, Nathan L. Anderson, and Alejandro Strachan

Effect of topological disorder on structure, mechanical, and electronic properties of amorphous silicon nitride: An atomistic study

Ravi Pramod Vedula,[1] Nathan L. Anderson,[2] and Alejandro Strachan[2*]

[1]School of Electrical and Computer Engineering, Purdue University, West Lafayette, Indiana

[2]School of Materials Engineering, Purdue University, West Lafayette, Indiana

ABSTRACT:

We present a first principles study of the effect of atomic variability on the structure, mechanical and electronic properties of amorphous silicon nitride. Using a combination of molecular dynamics and density functional theory calculations we predict an ensemble of statistically independent, well-relaxed and stress-free amorphous silicon nitride structures. We analyze the short, intermediate, and long-range order of the structures generated using radial distribution functions, ring statistics, bond angle distributions, and translational invariance parameters. Though energetically very similar, these structures span a wide range of densities (2.75-3.25 g/cm^3) and bulk moduli (115GPa to 220 GPa) in good agreement with the fabrication-dependent experimental range. Chemical bonds and atomic defects are identified via a combination of bond distance cutoff and maximally localized Wannier function analysis. A significant number of the amorphous structures generated (~30%) are defect-free providing an ideal reference to characterize the formation energy of the various point defects and their defect energy levels. An analysis of the Kohn-Sham density of states and energetics of the structures reveals that defects in amorphous dielectrics have a distribution of associated properties (e.g. formation energies and electronic energy levels) due to variations in local atomic structure; this should be taken into consideration in physics-based continuum models of these materials.

---

[*] Corresponding author: strachan@purdue.edu

I. INTRODUCTION

Amorphous silicon nitride (a-Si_3N_4) and its variants (a-SiN_x) are an important class of insulating materials used in various applications because of their electronic properties, high resistance to impurity diffusion, and ease of fabrication.[1] In addition to their use in silicon-oxide-nitride-oxide-silicon (SONOS) structures for non-volatile memory applications,[2] they are also widely used as a dielectric in radio frequency Microelectromechanical system (RF-MEMS) switches,[3-5] anti-reflective coating in silicon solar cells,[6, 7] passivation layer to form alkali-ion diffusion barrier[7] and dielectric insulator film for thin film transistors (TFT).[8] The amorphous SiN_x matrix is highly constrained due to its high overall coordination number and, hence, exhibits a high concentration of defects as compared to other amorphous dielectrics such as a-SiO_2.[9] These structural defects lead to electronic energy levels within the band-gap, which can trap charges and degrade its electronic properties for most applications.

A variety of fabrication techniques, including low pressure chemical vapor deposition,[10] reactive sputtering,[11] plasma discharge,[12, 13] and distributed electron cyclotron resonance plasma-enhanced chemical vapor deposition (DECR PVD)[14] are used for a-Si_3N_4 in specific applications. Depending on the variations in fabrication process, a wide range of structural, mechanical and optical properties have been reported in the literature. Densities between 2.6 to 3.2 g/cm^3 [15-17] and bulk moduli between 100 to 190 GPa[18] have been observed experimentally in a-Si_3N_4; these ranges remain theoretically unexplained.

The electronic properties of this class of materials is not fully understood either. Extensive experimental studies based on electron paramagnetic resonance (EPR) investigations have associated the charge trapping centers to the existence Si and N dangling bonds.[19-24] A combination of optical absorption spectra and EPR measurements indicate that the Si dangling bond contributes to trap energy level at approximately 2.8eV below the conduction band (CB).[23, 24] Analyzing the electrical conduction measurements using Poole-Frenkel mechanism models to determine trap depths showed the existence of two different slopes in the same sample indicating existence of two different trap depths.[25] More recent trap spectroscopy by charge injection and sensing experiments(TSCIS) and back extraction using charge pumping methods indicate that trap levels in stoichiometric a-Si_3N_4 span a range of energy levels between 0.8-1.8eV from the CB edge with a distinct peak at 1.6 eV below the CB edge.[26] While these experiments have been used to qualitatively associate the trapping centers with Si dangling bonds, a direct relationship between atomic defects, their charge states, and position of trap levels is still to be fully established. Also, the inherent variability associated with structure of the amorphous materials leads to large variabilities in the location of trap levels, making the experimental characterization of full range of these trap levels quite challenging. On the other hand, theoretical calculations based on classical and *ab initio* molecular dynamics (MD) and Monte Carlo methods have been used to model a-Si_3N_4 and its variants.[27-36] While structural, electronic, and vibrational properties based on these models have been extensively reported, comprehensive models capturing the effect of inherent local variability in the atomic structure and topological disorder of a-Si_3N_4 are still lacking. Consequently, theoretical predictions of trap depths based on these models report few distinct levels in the band-gap, as opposed to a range of values as expected from the atomic variability of the amorphous network[37] and reported in recent TSCIS measurements.[26]

In this paper, we generate and analyze an ensemble of well-equilibrated, statistically independent, a-Si_3N_4 structures to characterize the effect of local variability on the structure, mechanical, and electronic properties. Such an ensemble-based approach provides an effective approach to capture the statistical distribution of structural and electronic properties of amorphous systems. Similar approaches have been effectively used by other researchers for characterizing structural properties and defect formation energies in amorphous silica.[37-40]

We use a combination of MD simulations with empirical potentials and *ab initio* structural relaxations to generate the ensemble of well equilibrated, stress-free stoichiometric *a*-Si$_3$N$_4$ structures. Slow annealing via classical MD simulations followed by density functional theory (DFT) optimization leads to structures with small density of defects and several defect-free ones. By using both ring distributions and translational invariance analysis, we classify the generated structures into amorphous, semi-crystalline, and crystalline. A detailed bond analysis enables us to characterize the nature of the common defects in *a*-Si$_3$N$_4$, compute their average formation energies and corresponding electronic properties.

The paper is organized as follows: In section II we discuss the computational method used to predict the structures. In section III we describe the structural properties and report a classification scheme for the structures generated. In section IV we report and discuss the energetics and thermo-mechanical properties of the *a*-Si$_3$N$_4$ structures. In section V and VI we describe the atomic defects in the predicted structures, their formation energy, and their effect on the density of states (DoS). Finally, our conclusions are presented in section VII.

II. COMPUTATIONAL METHODS

A. MD and DFT calculation details

Our MD simulations use a modified Born-Mayer-Huggins (BMH) force-field that describes atomic interactions as a sum of two and three body terms to represent potential energy of the system.[41] This force-field used was parameterized with crystalline β-Si$_3$N$_4$ to generate Si-N and N-N interactions, with Si-Si parameters obtained from oxide potentials.[41] The potential was shown to generate representative amorphous structures, with structure properties consistent with experimental data and was used to study the effect of interphase mixing of silicate inter-granular films at the grain boundary interface of crystalline Si$_3$N$_4$. [41, 42] All the MD simulations are performed using the LAMMPS software package.[43] A Nose-Hoover thermostat and barostat with coupling constants of 0.01ps and 0.1ps respectively is used for these simulations.

Full DFT structural optimization (relaxing both atomic positions and cell parameters) is performed on the structures obtained from MD simulations using the Perdew, Burke and Ernzerhof (PBE) formulation of the generalized gradient approximation (GGA).[44] We use Quantum Espresso, an open source plane-wave DFT code, with an ultrasoft pseudopotential with nonlinear core correction for N and a norm conserving pseudopotential with nonlinear core correction for Si to describe core electrons.[45] We use a kinetic energy cutoff of 30 Ry and 240 Ry for the wavefunction and charge density respectively. A Γ-point sampling was used to perform Brillouin zone integrations. Convergence criterions of 1.36 x 10^{-4}eV, 2.5x10^{-2}eV/Å, and 5x10^{-2}GPa are used for self-consistent field (SCF) convergence, force relaxation, and stress relaxation respectively. Diagonalization was performed using conjugate gradients algorithms, and BFGS optimization algorithms were used for force and stress relaxations. All the calculations assume zero spin. To estimate the uncertainties in our predictions, we repeated the calculations within the local density approximation (LDA) of Perdew and Zunger[46] and using SeqQuest code, an atomic basis sets code from Sandia National Laboratories, with Troullier Martin pseudopotentials.[47] Consistent results were obtained using all approaches. The results presented below correspond to simulations using the Quantum Espresso code within the GGA approximation, unless mentioned otherwise.

B. Generation of an ensemble of *a*-Si$_3$N$_4$ structures and property prediction

To efficiently and accurately predict amorphous structures and their properties, we use a two-step method: i) Classical MD simulations with empirical interatomic potentials to generate an ensemble of trial amorphous structures by slow annealing of liquid samples; and ii) DFT force and stress relaxation starting from the MD structures to refine the MD atomic structures and obtain their cohesive energies, bulk moduli, and electronic properties. The computational efficiency of MD with interatomic potentials allows us to adequately explore the configurational space and generate a large number of statistically independent structures. The final structural refinement leads to fully relaxed DFT structures and energetics, and allows the characterization of their electronic structure. This methodology was applied previously to Si nanotubes[48] and a-SiO$_2$,[37] where as in a-Si$_3$N$_4$, it is important to consider an ensemble of structures to adequately account for local variability and topological disorder found on experimental scale.

We start from α-crystalline Si$_3$N$_4$ structural configuration consisting of 112 atoms in the supercell and heat it to T=12,000K (above the melting temperature as predicted by the potential) using isothermal and isobaric ensemble (NPT) MD simulations at a rate of 10K/ps to create a liquid structure. We obtain 60 independent liquid structures by sampling a 10ns-long canonical ensemble (NVT) MD simulation at the intrinsic liquid density (ρ=2.4g/cm^3) and T=12,000K. A nearest neighbor analysis and coordination statistics shows that the different liquid structures are statistically independent. Each of these 60 liquid structures is further equilibrated under NVT conditions for 10ps at different densities: intrinsic liquid density (2.4 g/cm^3), 2.7g/cm^3, 2.9 g/cm^3, 3.1g/cm^3 and 3.3 g/cm^3. The resulting structures are then cooled down to room temperature under NVT conditions (for the densities: 2.7, 2.9, 3.1 and 3.3g/cm^3) and NPT conditions (starting with intrinsic liquid density) at a cooling rate of 0.1K/ps. We examined different cooling rates (10K/ps, 1K/ps, 0.5K/ps and 0.1K/ps) for initial test simulations and found cooling rate to have a significant impact on the resulting structures. The slowest cooling rate leads to structures with lower energies and lower defect concentration; thus, all the results below correspond to 0.1K/ps cooling. Annealing at fixed densities leads to stress build-up and the resulting structures are further equilibrated under constant temperature and stress conditions at T=300K and 1 atm to obtain fully relaxed statistically independent a-Si$_3$N$_4$ models. Finally, we relax the MD structures using DFT energy minimization (atomic coordinates and simulation cell parameters, including angles, are relaxed). As explained in the following section, this procedure results in an ensemble of 207 stress-free, well-relaxed amorphous Si$_3$N$_4$ structures. All structures are available electronically in the supplementary material[49] and some representative structures are available for free online simulations in the SeqQuest tool in nanoHUB.org for online simulation.[47] To facilitate easy tracking of the structures generated, we identify each structure by the annealing density followed by the structure number (for example, 2.7S1 refers to ensemble structure number 1 generated at an annealing density of 2.7g/cm^3).

While the structures generated via the various processes lead to independent structures spanning a range of densities, those obtained at an anneal density of 3.3 g/cm^3 collapse into a single structure, with the same density and cohesive energy of one of the structures from the 3.1g/cm^3 anneal. Thus, the structures corresponding to this high-density anneal will not be considered further. Cooling under different mechanical constraints (different densities) is performed to more effectively sample the ensemble of possible amorphous structures and is not intended to mimic specific fabrication processes. This is motivated by our objective to characterize the molecular origin of the variability in reported densities and stiffness in these materials.

III. STRUCTURE CLASSIFICATION AND ANALYSIS

A. Structure characterization and classification

Before discussing the mechanical and electronic properties of the ensemble of predicted structures we analyze the resulting atomic configurations. Visual inspection of these structures generated indicated that a few structures exhibited long range order along specific directions (see Supplementary material section S2 for a snapshot and analysis of these structures). To quantify the long-range order and eliminate crystalline structures from the ensemble we use a combination of ring statistics and translational symmetry analysis. This allows us to classify the structures into amorphous, semi-crystalline, and crystalline.

A characteristic feature of crystals is the presence of translational symmetry. We quantify the translational symmetry parameter of the structures within the simulation cell using the following procedure. Each vector separating like atoms (two Si or two N atoms) in the structure is a potential translational symmetry operation; for each of these vectors we compute the number of sites that remain invariant after the translation operation is performed, i.e., the number of overlapping atoms (with a tolerance of 0.1 Å) considering their type, before and after the translation. We define the participation ratio for each translation vector as the ratio between the number of invariant atoms and the total number of atoms in the cell (N). A perfect crystal will have a participation ratio of 1 for all the vectors that represent a translational symmetry. On the other hand, an amorphous material will exhibit no vector with a large participation ratio. We define the number of non-periodic vectors as the number of vectors separating two like atoms that lead to participation ratios of $1/N$ (that is, where only the original pair remain unchanged after the translation). The percentage of non-periodic provides great insight into the character of our structures, as can be seen from the histogram in Fig. 1 for the ensemble of structures obtained from 3.1 g/cm^3 annealing. Clearly, two groups of structures can be identified: crystalline structures with a percentage of non-periodic vectors close to zero and disordered ones with the large percentage of non-periodic vectors. Similar trends can be observed for other annealing densities also.

Additional information about the structures, in particular their intermediate-range order and connectivity, can be obtained by ring statistics analysis. We use an algorithm by Yaun and Cormack [50] to obtain these primitive ring size distributions. Since we are dealing with stoichiometric systems with alternating Si and N atoms, the ring statistics are computed considering only the Si atoms. This analysis is important since amorphous structures are known to exhibit a wide distribution of primary ring sizes, contrary to crystals where only a few primitive ring sizes are observed. Figures 2(a-d) show the ring size distribution of the DFT-relaxed structures from different annealing procedures compared to ring distributions of the known crystalline polymorphs of Si_3N_4 (α-Si_3N_4 and β-Si_3N_4 ($P6_3/m$)). We see that many of the structures generated show broad ring size distributions as opposed to crystalline structures; for example, ring statistics of β-Si_3N_4 contains only 3, 4 and 6 membered primitive rings.[51] Thus, based on the translational symmetry analysis and ring statistics analysis we classify each of the structures into three categories:

Amorphous Structures: percentage of non-periodic vectors greater than 70% and probability of finding any n-sized primitive ring less or equal than 0.35 for all sizes;

Semi-crystalline structures: percentage of non-periodic vectors greater than 70% and at least one n-sized primitive ring with probability larger than 0.35;

Crystalline structures: otherwise.

Additional information about the classification of each structure can be found in the supplementary material.[49] The structural analysis in Figs. 1 and 2 show that our MD-DFT approach generates a large number of amorphous and semi-crystalline structures for all annealing conditions used and a few crystalline structures. Our results show that generating an ensemble of statistically independent a-Si$_3$N$_4$ structures using very slow cooling rates (by MD standards) results in a fraction of the structures being crystalline. Increasing the cooling rates (0.5 K/ps, 1 K/ps and 10K/ps) for a representative selection of these initial liquid structures (resulting in crystalline structures for cooling rate of 0.1K/ps) leads to all amorphous configurations. However, as explained above, using a cooling rate of 0.1 K/ps results in structures with lower energies and lower concentration of defects, and hence we use this ensemble in the remainder of the paper; the crystalline structures will not be considered further, except to compute amorphization energies, since our focus is on amorphous Si$_3$N$_4$. While the distinction between semi-crystalline structures and amorphous structures based on cutoff of probability of primitive rings >0.35 is arbitrary, it does not affect our results since we consider both semi-crystalline and amorphous structures for subsequent analysis. As expected, the amorphous structures in the ensemble contain wide ring size distributions ranging from 3- to 12-member rings. Figure 2(a) shows that the amorphous structures obtained from NPT cooling contain rings with more than 10 members indicating open structures. These have been found to be porous and highly defective; representative snapshots of these structures are shown in section S3 of the supplementary material. Therefore, these structures are not relevant for electronic applications and hence they will not be considered below, except when specifically mentioned.

In summary, the structural analysis shows that annealing at constant densities of 2.7 g/cm^3, 2.9 g/cm^3, and 3.1 g/cm^3 generate an ensemble of porous-free amorphous structures relevant for applications where high-quality dielectrics are needed. Annealing at lower or higher densities does not result in additional structures with desired characteristics. After removing crystalline and porous structures we are left with 152 crystalline and semi-crystalline structures whose structures and properties will be analyzed in the remainder of the paper.

B. Radial Distribution Functions

We calculate radial distribution functions (RDFs) and angle distributions to compare structural details of the models generated against experimental data and validate our predictions. Table 1 summarizes, among other properties, ensemble averages of the peak positions for the pair correlation functions and angle distributions of all the amorphous and semi-crystalline structures generated. The total RDFs are obtained from the fully relaxed DFT structures and averaged for those originating from each annealing density, see Fig. 3. A bin size of 0.02 Å was used for calculating the RDF. The first peak corresponding to Si-N bonds at 1.75 Å is in good agreement with X-ray diffraction peak value of 1.75 Å.[15] The peak position and its associated standard deviation of 0.05 Å indicates that the majority of bonds are comparable to bond-length of 1.74 Å in β-Si$_3$N$_4$; supporting the argument of short range interactions are very close to β-Si$_3$N$_4$. The second peak of the RDF corresponds to a combination of N-N and Si-Si inter-atomic distances. Since the experimental RDF data of stoichiometric a-Si$_3$N$_4$ is available only for densities 2.6 g/cm^3 and 2.87

g/cm^3, the RDF is compared to the nearest experimental density. The ensemble averaged partial RDFs for anneal density are presented in the supplementary material. In Fig. 4 we plot the ensemble averaged Si-N-Si and N-Si-N bond distributions for the structures generated using different annealing conditions. The Si-N-Si bond distribution peaks at around 118° with standard deviation of about 13.4°. This variability in Si-N-Si bond angle leads to topological disorder. The Si-N-Si bond angle distribution provides insight into the structure beyond the short-range order. The N-Si-N bond angle distribution peaks at around 110° with a standard deviation of about 16.4°. This value is close to N-Si-N bond angle crystalline β-Si$_3$N$_4$of 109.47°. In addition to the main peaks, we find that angle distributions also show distinct peak around 90°. This peak is due to presence of significant fraction edge-sharing tetrahedral in the network. The peak values of RDF and angle distributions obtained are in good agreement with data reported in the literature (see Table 1). [34]

IV. DISTRIBUTION OF COHESIVE ENERGY, DENSITY AND BULK MODULUS

Having classified and analyzed the structures, we now analyze their energetics. Figure 5 shows the cohesive energy per formula unit of all the DFT relaxed samples plotted against the final relaxed densities calculated as:

$$E_{coh} = \frac{E_{Si_3N_4}(n) - (3nE_{Si} + 4nE_N)}{n},$$

where $E_{Si_3N_4}(n)$ is the total energy of the amorphous cell with n Si$_3$N$_4$ units, and E_{Si} and E_N are the total energies of isolated Si and N atoms respectively. The results for our amorphous samples are compared against the DFT energy calculations for α-Si$_3$N$_4$ and β-Si$_3$N$_4$. In Fig. 5 closed symbols represent amorphous structures, stars represent crystalline structures and open symbols represent semi-crystalline structures. We find β-Si$_3$N$_4$ to be lower in energy by about 0.22 eV per formula unit than α-Si$_3$N$_4$ (green stars in Fig.5) in agreement with DFT calculations reported in literature.[52] The amorphization energy of our ensemble calculated with reference to α-Si$_3$N$_4$ is 1.07±0.28 eV per formula unit. This number is only slightly larger than the experimental value of 0.72±0.13 eV[53] indicating good relaxation; by comparison, prior DFT-based predictions predict an amorphization energy of 2.8 eV per formula unit with respect to β-Si$_3$N$_4$.[30, 31] The crystalline structures generated from 3.1 g/cm^3 annealing are energetically very similar to α-Si$_3$N$_4$ crystalline polymorph and also exhibit similar ring statistics, Fig. 2(d), and RDF, see supplementary material.[49] Similarly the ring distributions of crystalline structures from 2.7 g/cm^3 melt density resemble the β-Si$_3$N$_4$ crystalline polymorph [Fig. 2(b)], though they exhibit higher energy and a lower density, indicating the possibility of distorted β-Si$_3$N$_4$ crystalline polymorph. The fact that our MD annealing followed by DFT relaxation approach leads to crystalline structures that closely resemble the known crystalline polymorphs and also predicts the amorphization energy in agreement with experimental values are good measures of the validity of the approach.

Our simulations show that stress-free amorphous or semi-crystalline Si$_3$N$_4$with similar energetics exhibit a wide range of densities, see Fig. 5. The range of predicted densities for these structures (from 2.75 to 3.25 g/cm^3) is in good agreement with experiments, where densities ranging from 2.6 to 3.2 g/cm^3 have been reported.[15-17] We note that structures annealed at lower or higher densities do not result in additional amorphous structures. As mentioned earlier, we believe the structures from the NPT anneal are not experimentally relevant for electronic applications (CVD or PECVD generated) and will not be considered any further. Interestingly, a-Si$_3$N$_4$ produced using pyrolysis or sol-gel methods, has a density

of 2.27-2.44 g/cm^3, consistent with the predictions from NPT anneal density.[54] The accurate prediction of the range of experimental densities is unprecedented and represents a key validation of our approach.

We now analyze the bulk moduli of the ensemble of generated amorphous and semi-crystalline structures. For bulk modulus predictions, we compute energy-volume curves from force relaxation calculations of the structure with the cell dimensions scaled isotropically from -5% to +5%. Atomic positions are relaxed at each level of volumetric strain. Figure 6 shows the histogram of bulk modulus obtained from the ensemble of structures. As with densities we find that the intrinsic variability in atomic structure of the amorphous structure leads to a wide range of properties; the values predicted are in good agreement with the range of experimental bulk moduli (100 and 190 GPa) [18] and also agree well with the DFT predictions in Refs. [30-32]. We see that the bulk moduli of the structures increase, in average, with increasing density. Prior work on stoichiometric a-Si$_3$N$_4$ focused on a single structures with density between 3.1 and 3.2 g/cm^3 [29, 34] or a small number of structures with various densities.[30-33] In contrast, our ensemble approach predicts distributions of densities and elastic properties for stress-free stoichiometric a-Si$_3$N$_4$ in agreement with experimental observations.

V. ATOMIC STRUCTURE OF POINT DEFECTS a-Si$_3$N$_4$ AND DISTRIBUTION OF FORMATION ENERGIES

A. Defect identification

Topological defects in a-Si$_3$N$_4$ are defined with reference to a defect-free structure, which is a continuous network of alternating Si and N atoms with respective coordination of four and three. Deviations from this ideal coordination are considered defects. Our approach to identify and classify defects is based on pairwise-distance-based criterion to compute the number of bonds for each atom using a cutoff radius, augmented by insight obtained from a Wannier function analysis. A cutoff radius of 2.2 Å is used for the defect analysis; this is close to the minimum between the first and second peaks of the RDF and leads to lowest number of defects. A distance-based criterion has the advantage of simplicity and computational efficiency but it fails to acknowledge the actual electronic structure of the system. Hence, we complement the cutoff-based approach with a detailed analysis of the electronic wavefunctions that can accurately establish the presence and nature of bonds. Maximally localized Wannier functions (MLWF)[55, 56] is one such scheme and we apply it to identify topological defects accurately.

In addition to undercoordinated and over-coordinated defects, a number of *ab initio* derived models report the presence of wrong bonds (N-N or Si-Si bonds) [30, 31, 35] based on a geometric criterion, these are commonly reported in edge-sharing tetrahedron. Also, recent MD simulations with empirical potentials find shorter N-N bonds and postulate them to explain a small peak in the neutron diffraction experiments.[36] Figure 7 shows two such configurations of edge sharing tetrahedron with Si-Si and N-N bond distances considerably shorter than usual Si-Si and N-N bond lengths in a-Si$_3$N$_4$, indicating possible existence of these wrong bonds. In order to confirm whether these nearby N and Si atoms form real chemical bonds or not, we performed an electron localization analysis on a few such structures using MLWF. A Wannier function center (WFC) between Si and N atom along the line bonds represents a sigma bond.[56] The MLWF analysis, with WFC shown in Fig. 7 as small green spheres, indicates no chemical bond between the Si-Si and N-N atoms. All other bonds identified by the pairwise analysis are

confirmed by our MLWF analysis. A more detailed description of the MLWF analysis is provided as supplementary material.

From this insight, we add the following rule to the pairwise analysis: Si-Si and N-N bonds between overcoordinated atoms are ignored if the atoms involved are two corners of an edge sharing tetrahedron. We will refer to this approach as Wannier localization informed bond analysis. A similar method was used by Jarolimek *et al.* [35] and our analysis provides a rigorous justification based on a wave function analysis.

B. Defect characterization

Our analysis shows that Si and N atoms with one additional or missing bond are the most common defects; under- and overcoordinated Si atoms will be denoted III-Si and V-Si respectively; similarly defective N atoms will be denoted II-N and IV-N. In all our simulations we find defects occurring in pairs. This can be explained by considering that if only atoms with coordination numbers that differ from their perfect values by one are considered; creating or breaking a bond in the network changes the total number of defects by two or leaves it unchanged. Out of the 152 amorphous and semi-crystalline structures of interest here, 29.87% are defect free, 7.79% contain a single defect pair, and the rest 62.34% contain multiple defect pairs.

Figure 8 shows the number of undercoordinated [Fig. 8(a)] and overcoordinated [Fig. 8(b)] atoms in the simulation cells as a function of their density. Despite the large scatter originating from atomic variability from structure to structure, Figs.5 and 8 indicate that the structures with densities around 2.9 g/cm^{3}have, in average, lower energy and defect density; several of these structures (76% of those annealed at a density of 2.9g/cm^3) are defect-free. Interestingly, this corresponds to the experimental density of high-quality quasi-stoichiometric films generated using DECR PVD suitable for optical and electronic applications[14] (experimental density of 2.9±0.12g/cm^3). However, our simulations show that defect density is not a strong function of structure density in the 2.7-3.1 g/cm^3 range. While EPR experiments strongly suggest the existence of undercoordinated atoms (III-Si and II-N),[21] there is no direct experimental evidence for overcoordination defects in a-Si$_3$N$_4$. Similar observations for structural defects have been reported in previous studies.[33, 34] The slow anneals we use lead to a concentration of defects lower than in prior simulations and closer to the experimental values obtained from EPR and electrical conduction in a-Si$_3$N$_4$.[17, 21] We obtain 0.6% undercoordinated Si atoms, 1.1% undercoordinated N atoms and 2.0% overcoordinated atoms in average for the amorphous and semi-crystalline structures. While this is still higher than the experimental values of 10^{18}-10^{20}cm^{-3} [17, 21] our samples have lower defect concentrations than those reported in simulations to date, from 1% in Ref. [30, 31, 33] to 10.3% of III-Si atoms in Ref.[36]. The relatively small number of defects enables us to perform a detailed characterization of their formation energies and electronic properties, and the various defect-free amorphous structures generated provide an appropriate baseline for the quantification of these properties.

C. Distribution of defect formation energies

We now focus on the formation energy of the native defects present in the ensemble of structures. Since defects come in pairs in our stoichiometric cells and many cells exhibit multiple pairs we report the formation energy per defect pair. Figure 9 shows a histogram of the formation energy per pair (E_f) of topological defects in a-Si$_3$N$_4$ obtained as:

$$E_f = \frac{E_{def} - \langle E_{perf} \rangle}{n_{def}}$$

Where E_{def} is the total energy of a cell containing n_{def} defect pairs and the reference energy $\langle E_{perf} \rangle$ is the average total energy of the defect-free structures. Our simulations predict formation energies per defect pair between 0.5 and 5eV, as shown in Fig. 9. This large variability in the formation energies results from variability in local structure in the ensemble of structures and has been observed in other amorphous dielectrics.[37]

To our knowledge this is the first report of defect formation energy in a-Si$_3$N$_4$, so we compare our results to vacancy formation energy in crystalline Si$_3$N$_4$ ploymorphs and point defects in a-SiO$_2$. The heat of formation of the nitrogen vacancy in β-Si$_3$N$_4$ was calculated to be 3.6 eV and formation energy for point defects in amorphous SiO$_2$ were predicted to vary between 1.7 eV and 6.8 eV.[37] The lower defect formation energy in a-Si$_3$N$_4$ relative to a-SiO$_2$ explains the comparatively high concentration of defects observed experimentally in a-Si$_3$N$_4$ dielectrics compared to a-SiO$_2$, a similar and more commonly used dielectric for electronic applications.

VI. ELECTRONIC STRUCTURE AND ROLE OF DEFECTS

We now turn our attention to the effect of atomic defects on the band structure of the material; in particular we are interested in characterizing the energy levels within the bandgap induced by the various topological defects. Analyzing the ensemble of defective structures allows us to compute the distribution of trap levels of each defect type. These electronic defect states are critical in most electronics applications since they can trap charges, and are either desired or to be avoided depending on the application. Figures 10-11 show the Kohn-Sham (K-S) electronic DoS and projections of DoS over defective atoms for a variety of structures. A gaussian broadening of 0.1eV was used for calculating DoS and projected DoS. DFT energy levels are defined up to an additive constant and a rigid shift in energy scale of K-S spectrum is necessary for comparing the DoS of different structures. Hence, we align the average values of core energies (energy values corresponding to first band) from K-S energy spectrum for different systems.

Our defect analysis identified 46 defect-free amorphous or semi-crystalline networks; these structures are energetically very similar (Fig. 5) and their K-S DoS are also similar; thus, we use their average K-S DoS as a reference to compare the defective structures. Solid green lines in Fig. 10 show the DoS of the defect-free structures. To quantify the role of topological disorder and structure-to-structure variability on the electronic states we define our valence band (VB) edge to be at -5.92±0.2 eV and CB edge at -2.02±0.2 eV, see Figs. 10 and 11. The continuous set of energy levels adjoining highest occupied molecular orbital (HOMO) and lowest un-occupied molecular orbital (LUMO) of the defect-free structures were used to define the VB edge and CB edge respectively, and consequently K-S band-gap. The K-S bandgap is 3.9 ±0.4 eV; as is typically the case, this value is lower than the experimental value of 4.55 eV.[57] Having established a reference DoS we now focus on the electronic states contributed by some of the common defects. Projecting the DoS over the defective atoms enables us to characterize their individual

contributions. Figure 10 shows that III-Si atoms contribute states near the CB edge while undercoordinated N atoms (II-N) contribute states near the VB edge. On the contrary, overcoordinated atoms (V-Si and IV-N) do not contribute states within the bandgap. These results are in very good agreement with spectroscopic measurements and prior theoretical models.[21, 23, 24, 34] However, our ensemble approach enables us to characterize the distribution of energy levels and compare the theoretical predictions with reported by TSICS measured trap ranges. Figure 11 shows the distribution of trap levels in the bandgap contributed by every defect type. These distributions are obtained by averaging the projected K-S DoS on each defective atom classified by type. We find that localized states arising from III-Si atoms span a range of approximately 1.8eV right below the CB edge, as shown in Fig. 11. These results are in very good agreement with the TSCIS experiments on stoichiometric a-Si_3N_4 that report a range of energy levels between 0.8-1.8eV below the CB edge (energies below 0.8 eV could not be probed by the experimental setup). Similarly undercoordinated N atoms lead to band tail states around the VB edge or localized states close to VB edge spanning a range of 1eV, similar in width to the Si dangling bonds.

From these DoS calculations we can show that definite correlations exist between the states in bandgap and the coordination defects in the structure. More importantly, we find that specific defect types (defined by its atomic coordination) in amorphous materials do not contribute a single, sharp energy level within the bandgap, but a distribution of values due to variations in the local chemical environments, Figs. 10 and 11. This is also consistent with the observation of large fluctuations in the formation energy of the atomic defect for amorphous structures; see Fig. 9 and Ref.[37]

VII. CONCLUSIONS

We generated an ensemble of statistically independent, fully-relaxed, a-Si_3N_4 structures and characterized their structural features, stiffness, and electronic properties from first principles. Our approach captures the local variability in properties due to inherent, atomic-level structural variations of amorphous materials. The computational efficiency of the MD-DFT method used allows us to adequately explore configurational space and generate ensembles of representative structures. The quality of the ensemble of structures predicted depends, to a large degree, on the MD annealing and the accuracy of the force field used to compute atomic interactions. To assess the accuracy of our description we characterized the correlation between the total energies predicted for the ensemble of structures by the force field and DFT. The results, shown in Fig. S10, of the supplementary material, show a good correlation especially in the difference between the crystalline and amorphous structures, indicating that the force field does not artificially favor or penalize these two classes of structures.

Our simulations predict a variety of a-Si_3N_4 structures with similar energetics but a wide range of densities and bulk moduli. The predicted ranges of density and stiffness are consistent with the experimental range, reported for different fabrication conditions. An accurate defect analysis scheme taking electronic wavefunctions into account has been used for identifying chemical bonds in the structures. Structures generated have a considerably lower concentration of defects compared to prior theoretical work that we believe are more representative of high-quality samples. The predicted ensemble contains defect-free amorphous structures that provide an ideal baseline to quantify defect formation energies and their contributions to electronic states within the material's bandgap. We calculated the

formation energy for a pair of defects to be in the range of 0.5-5eV, comparable to formation energy of lowest energy defects in a-SiO$_2$.

We find that III-Si atoms contribute a distribution of energy levels that span about 1.8 eV below the CB edge and II-N contributes a slightly narrower distribution of states near the VB edge. On the contrary, overcoordinated defects do not lead to states within the bandgap. These distributions of states should be included in physics-based models of dielectric charging of a-Si$_3$N$_4$. For a more quantitative and in-depth analysis of the electronic properties of these defects, explicit GW calculations[58] or charge state calculations[59] would be necessary. Charge state calculations can not only provide more accurate energy levels, but also enable the characterization of structural rearrangements caused when defects trap electrons or holes. This paper provides insight of the physics of these defects and an ensemble of atomistic structures from which to build on in future calculations.
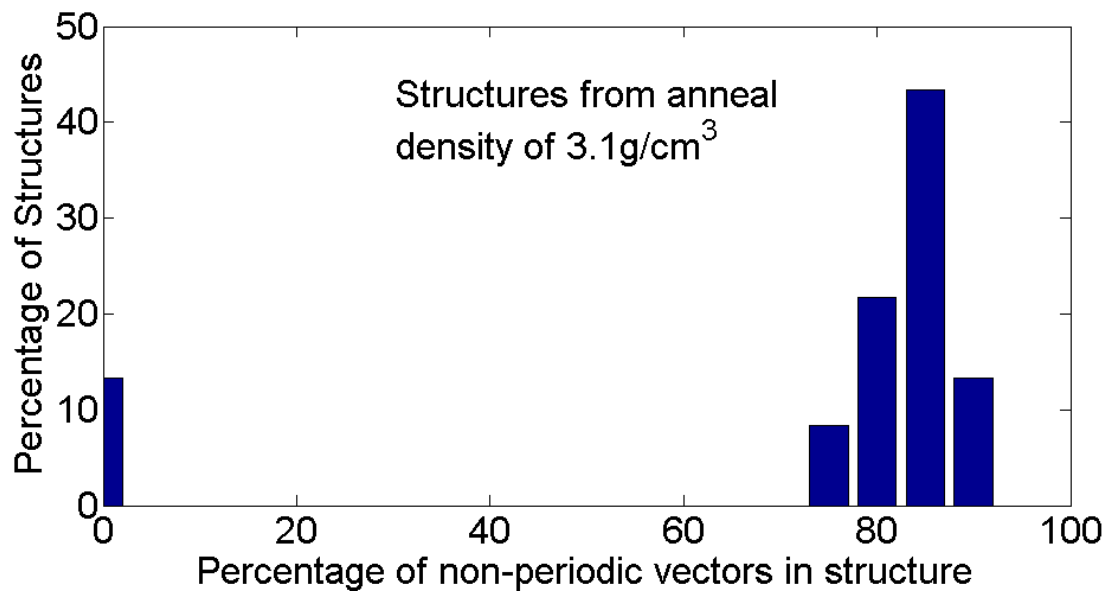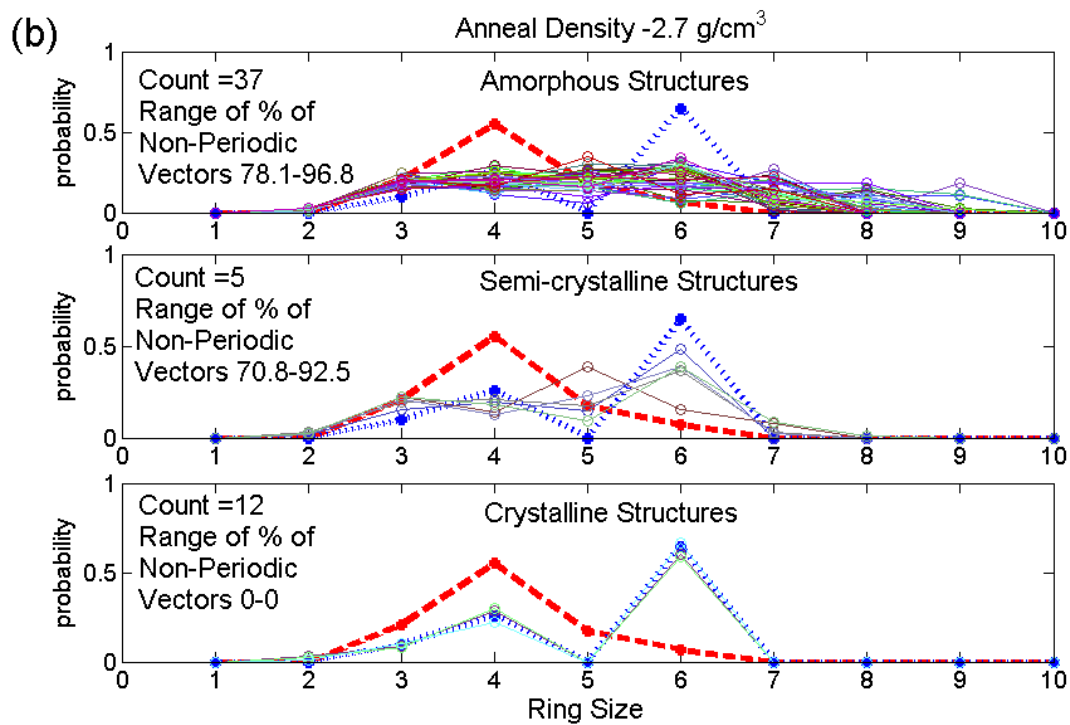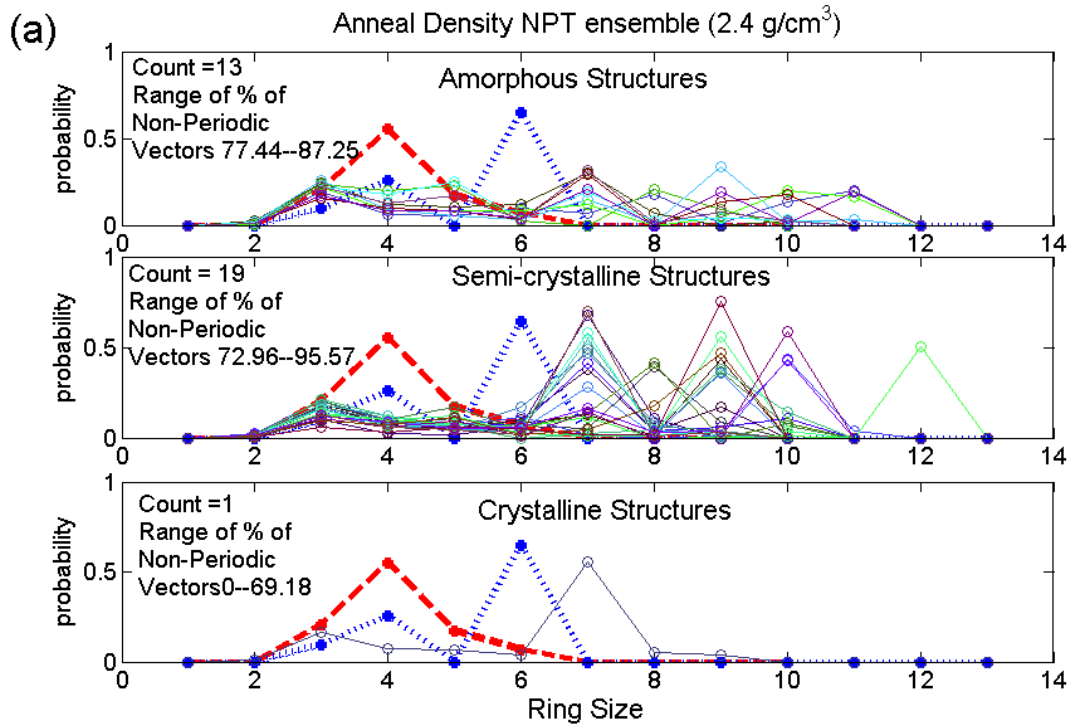
Figures:

Figure 1 (Color Online): Histogram of percentage of non-periodic vectors for the ensemble of structures obtained from 3.1 g/cm^3 annealing.
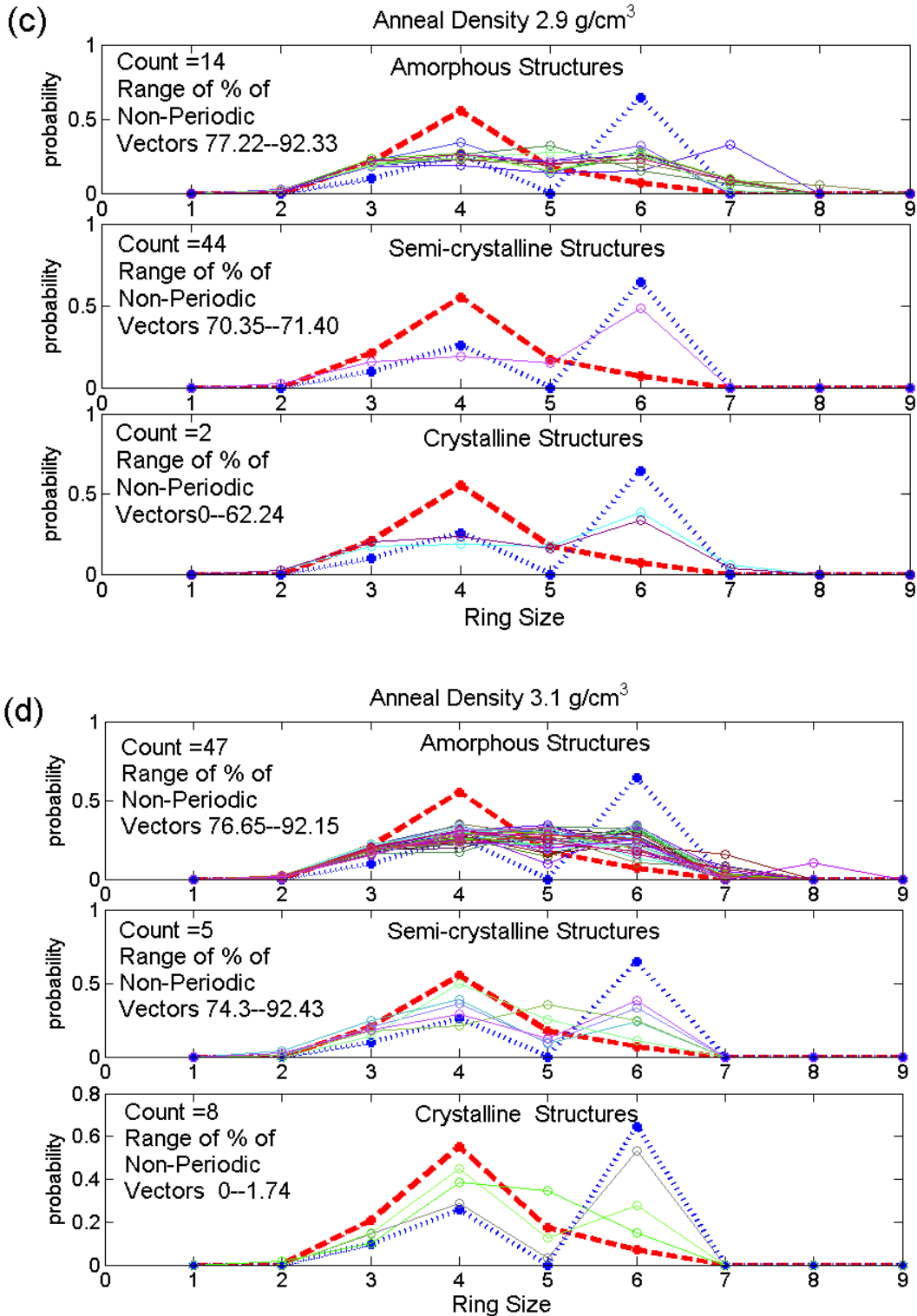
(a) Anneal Density NPT ensemble (2.4 g/cm^3)

Amorphous Structures

Count =13
Range of % of
Non-Periodic
Vectors 77.44--87.25

Semi-crystalline Structures

Count = 19
Range of % of
Non-Periodic
Vectors 72.96--95.57

Crystalline Structures

Count =1
Range of % of
Non-Periodic
Vectors0--69.18

(b) Anneal Density -2.7 g/cm^3

Amorphous Structures

Count =37
Range of % of
Non-Periodic
Vectors 78.1-96.8

Semi-crystalline Structures

Count =5
Range of % of
Non-Periodic
Vectors 70.8-92.5

Crystalline Structures

Count =12
Range of % of
Non-Periodic
Vectors 0-0

Ring Size

Figure 2 (Color Online): Ring statistics distributions of the final relaxed *a*-Si$_3$N$_4$ structures compared to the known crystalline polymorphs, α-Si$_3$N$_4$(red dashed line) and β-Si$_3$N$_4$ (blue dashed line). The subplots (a-d) represent the various initial annealing densities. All the final relaxed structures are classified into amorphous, semi-crystalline and crystalline structures.
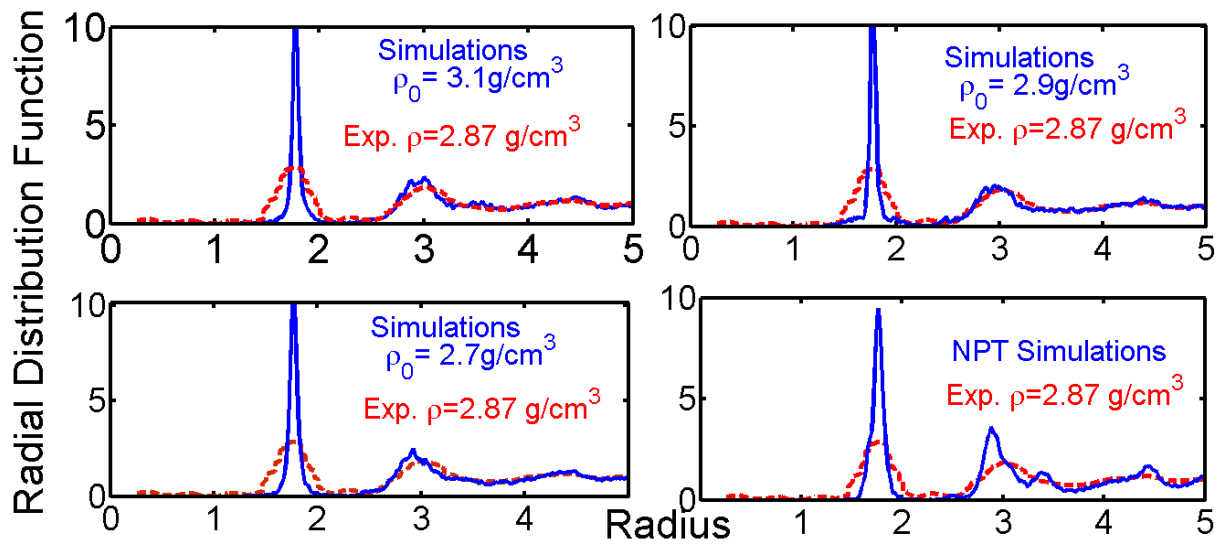
Figure 3 (Color Online): Comparison of ensemble averaged radial distribution function of stress relaxed *a*-Si₃N₄ samples (solid line) with RDF obtained from X-ray diffraction experiments (dashed line)[15]. The (ρₒ) in the subplot title indicates the annealing density of the ensemble at the start of MD-cooling simulations.
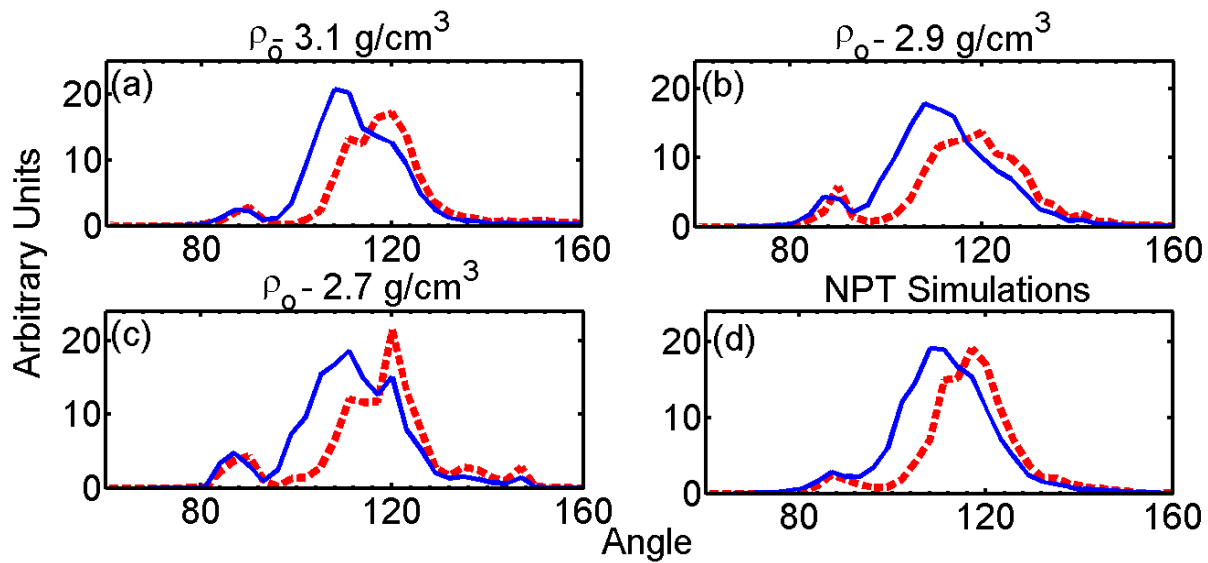
Figure 4(Color Online): Ensemble averaged N-Si-N(solid) and Si-N-Si(dashed) angle distributions of stress relaxed a-Si$_3$N$_4$ samples. The (ρ_o) in the subplot indicates the annealing density of the ensemble at the start of MD-cooling simulations.
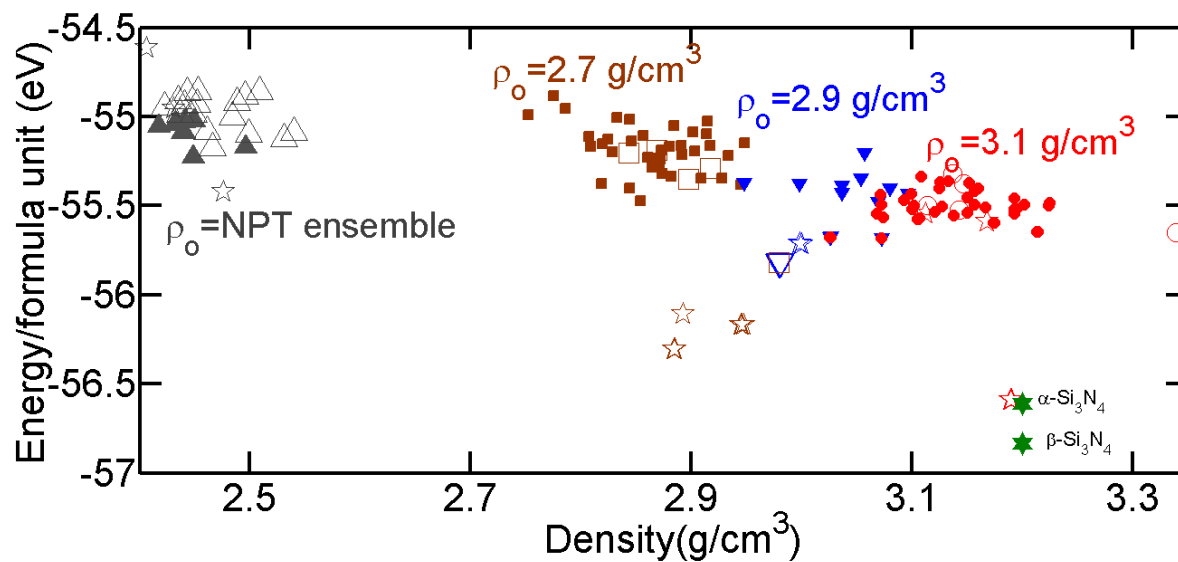
Figure 5 (Color Online): DFT-GGA cohesive energy calculated with reference to isolated atoms of the ensemble of annealedstructures as a function of their density. Filled symbols indicate amorphous structures, open symbols represent semi-crystalline structures and stars represent crystalline structures classified according to scheme presented. Filled green stars indicate known crystalline polymorphs. Different symbols represent structures generated at different annealing conditions.
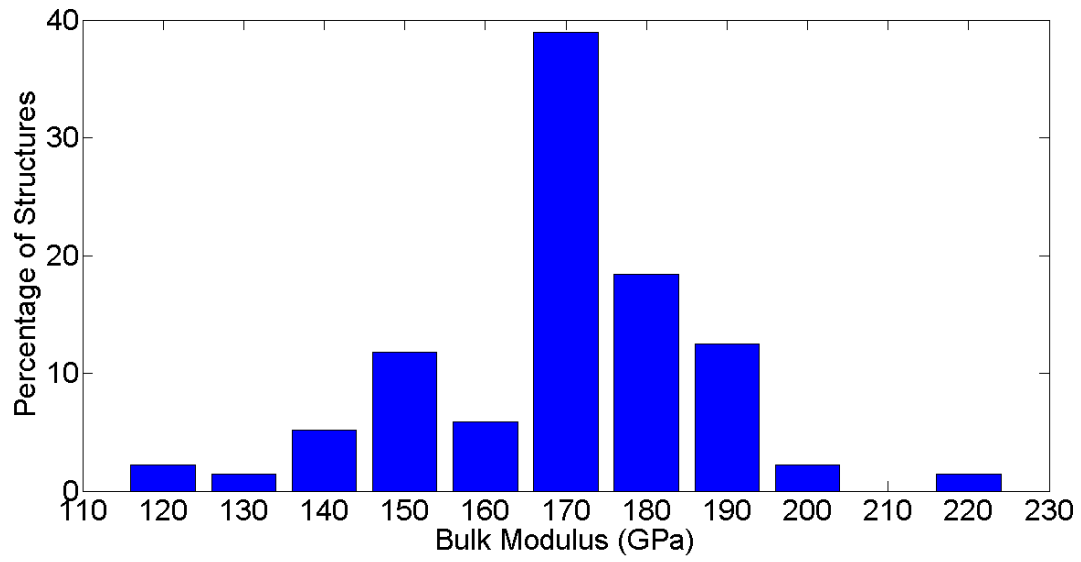
Figure 6 (Color Online): Histogram of bulk modulus calculations of stress relaxed a-Si$_3$N$_4$ samples.
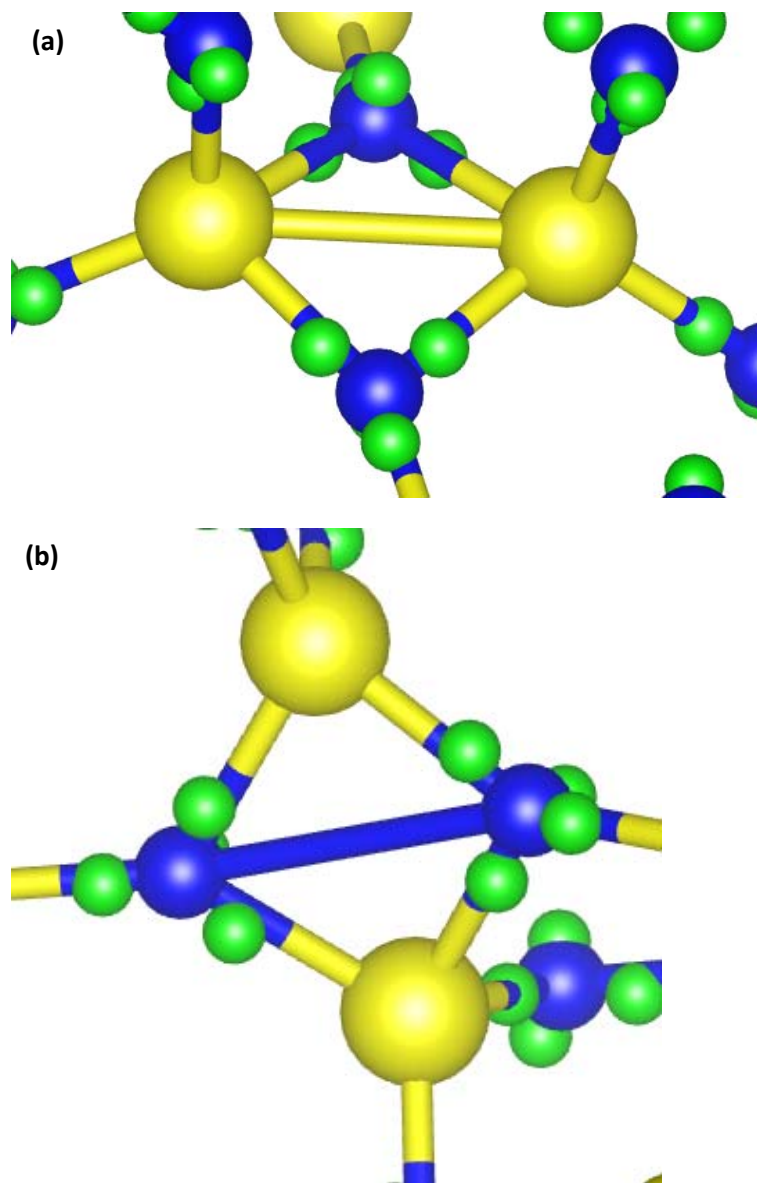
Figure 7(Color Online): (a) Snapshot of an edge sharing tetrahedron of a-Si$_3$N$_4$, with a spurious Si-Si bond detected by simple distance cutoff based analysis. The Wannier function centers (green, small spheres) between Si atoms (yellow, large spheres) and N atoms (blue) indicate the presence of chemical bonds. (b) Snapshot of an edge sharing tetrahedron in a-Si$_3$N$_4$, with a spurious N-N bond is detected by simple distance cutoff based analysis; Wannier analysis indicates this not to be a real chemical bond.
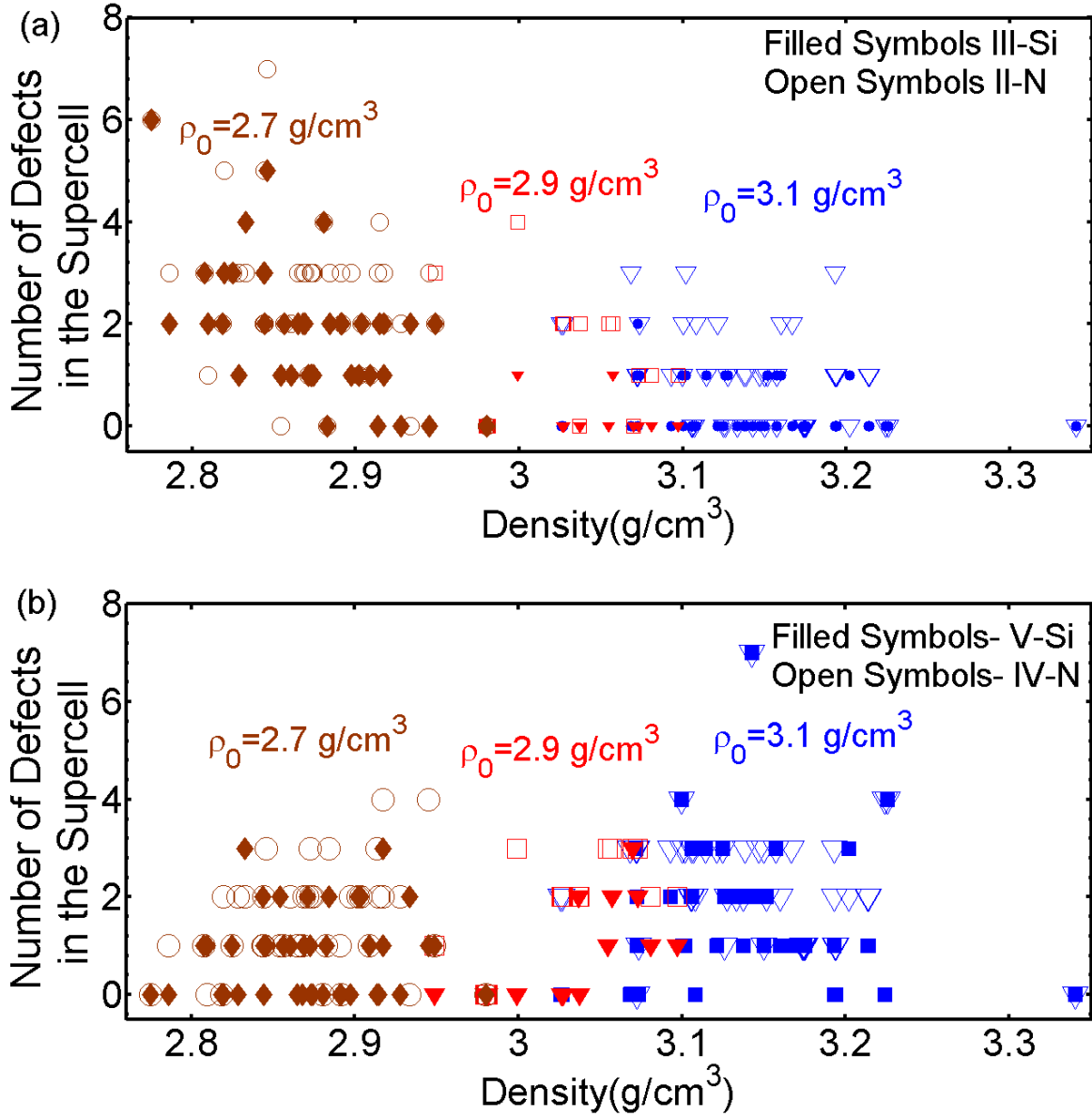
Figure 8 (Color Online): (a) Number of under-coordinated N and Si atoms (II-N and III-Si) (b) and over-coordinated atoms (IV-N and V-Si) for the DFT relaxed 112 atom *a*-Si₃N₄ structures as a function of density. Different symbols indicate the independent structures from ensembles generated from different annealing densities.
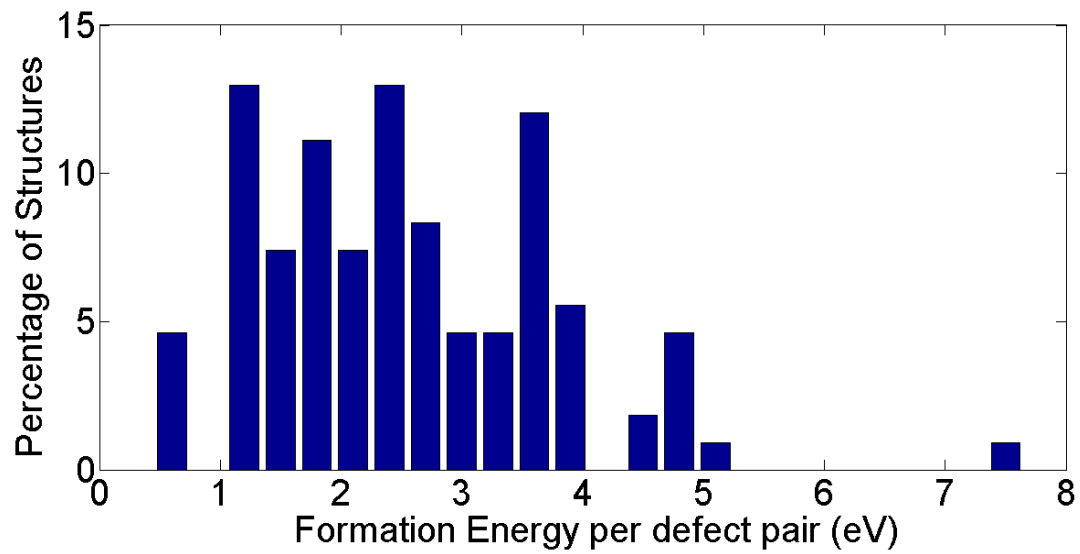
Figure 9 (Color Online): Histogram of formation energy per defect pair of stress relaxed *a*-Si₃N₄ samples.
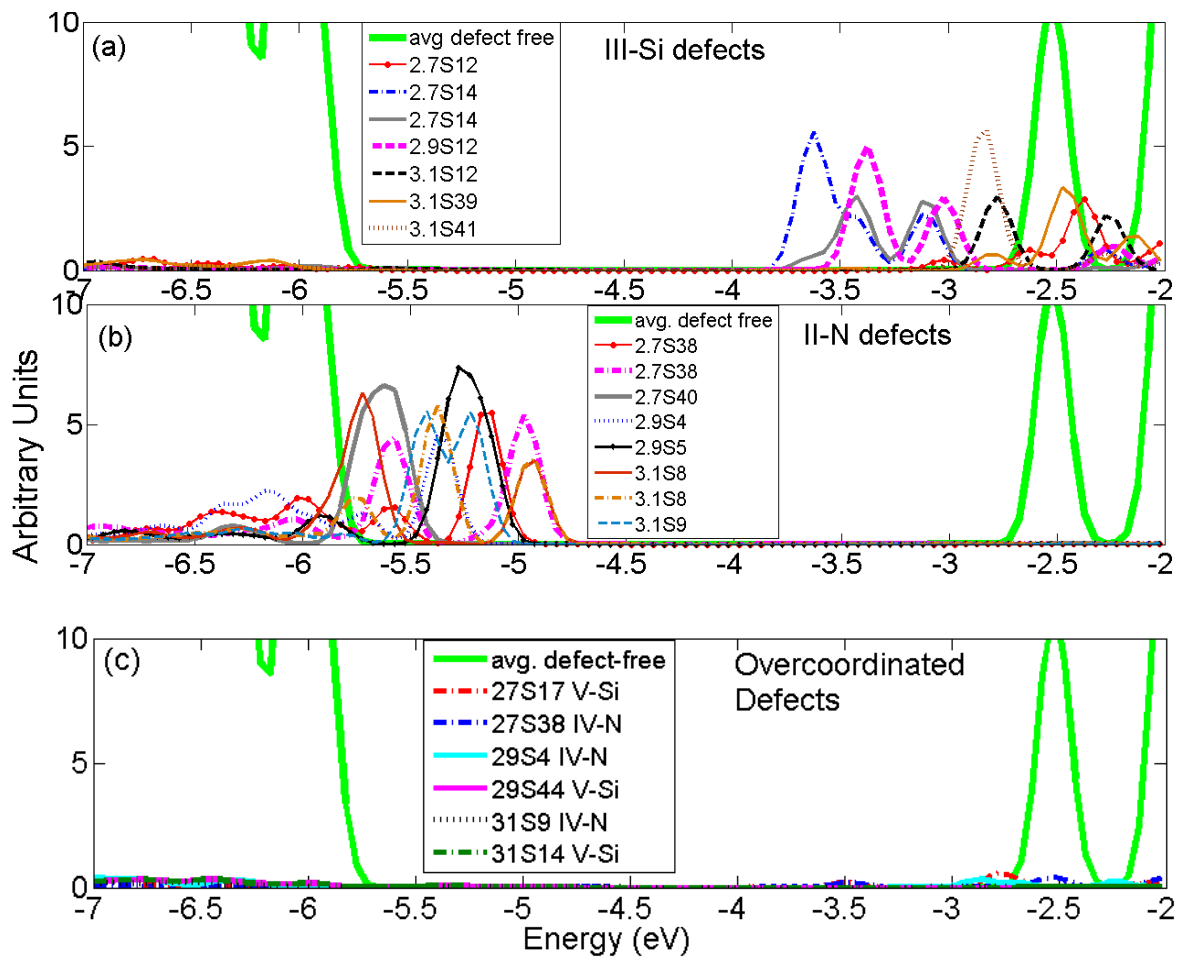
Figure 10 (Color Online): Variation in localized energy levels in band-gap for same defect type with different local environment. (a) Projected Density of States over under-coordinated Si bonds (III-Si) from statistically independent structures. (b) Projected Density of States over under-coordinated N bonds (II-N) from statistically independent structures. (c) Projected Density of States over over-coordinated Si and N bonds (V-Si and IV-N) from statistically independent structures.
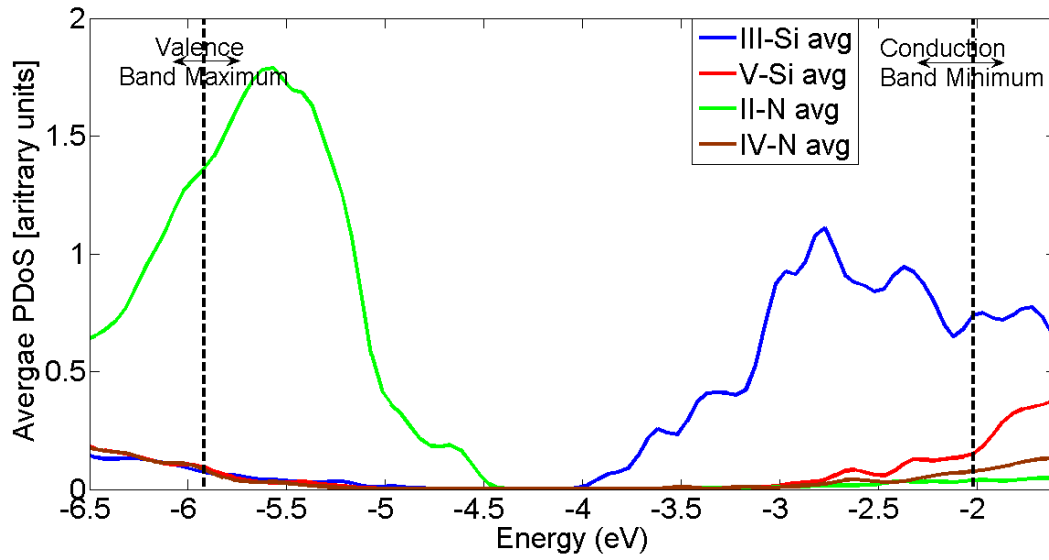
Figure 11 (Color Online): Average of Projected Density of States over all the independent realizations in the ensemble for each specific defect type (III-Si, V-Si,II-N and IV-N).

Table 1: Ensemble averaged structural properties for DFT relaxed amorphous and semi-crystalline structures are presented for different annealing densities. A comparison to the (a) X-ray diffraction experiments[15] (b) Neutron Diffraction experiments is presented[16]

Ensemble Average Quantity	ρ_o=2.4g/ cm^3	ρ_o=2.7g/ cm^3	ρ_o=2.9g/cm^3	ρ_o=3.1g/ cm^3	Experiments
1NN (Si-N) peak position	1.747±0.018 Å	1.748±0.016 Å	1.757±0.008 Å	1.754±0.009 Å	1.75[a]Å 1.73±0.004[b] Å
N-N peak position	2.847±0.027 Å	2.831±0.044 Å	2.841±0.03 Å	2.845±0.039 Å	2.83±0.006[b]Å
Si-Si peak position	2.998±0.047 Å	3.005±0.069 Å	3.02±0.03 Å	3.027±0.058 Å	3.01 [b] Å
Si-N-Si angle peak value	118.8±3.4°	115.9±3.5°	118.9±2.6°	115.8±3.5°	
N-Si-N angle peak value	109.3±1.5°	109±3.6°	111.6±3.7°	110.3±2.4°	
Density (g/cm^3)	2.44±0.06	2.86±0.05	2.99±0.03	3.14±0.06	2.6-3.2[a,b]
Cohesive Energy per formula unit(eV)	-54.99±0.13	-55.2±0.16	-55.74±0.158	-55.52±0.09	
Bulk Modulus(GPa)		148.34±13.65	169.33±3.15	183.76±11.54	100-180 [18]

REFERENCES:

[1]   T. P. Ma, IEEE Trans. Electron Devices **45**, 680 (1998).

[2]   M. H. White, D. A. Adams, and J. Bu, IEEE Circuits Devices Mag. **16**, 22 (2000).

[3]   G. Papaioannou, M. Exarchos, V. Theonas, G. Wang, and J. Papapolymerou, IEEE Trans. Microwave Theory Tech. **53**, 3467 (2005).

[4]   X. Yuan, J. Hwang, D. Forehand, and C. Goldsmith, *2005 IEEE MTT-S International. Microwave Symposium Digest*, Long Beach, CA, 12-17 June, 2005 (IEEE, New York, 2005), pp. 753–756.

[5]   J. W. Lee, A. K. Mahapatro, D. Peroulis, and A. Raman, J. Microelectromech. Syst. **19**, 1490 (2010).

[6]   C. Leguijt, et al., Sol. Energy Mater. Sol. Cells **40**, 297 (1996).

[7]   B. S. Richards, Prog. Photovoltaics **12**, 253 (2004).

[8]   G. Lavareda, C. N. de Carvalho, A. Amaral, E. Fortunato, A. R. Ramos, and M. E. da Silva, Thin Solid Films **427**, 71 (2003).

[9]   G. Lucovsky, Y. Wu, H. Niimi, V. Misra, and J. C. Phillips, Appl. Phys. Lett. **74**, 2005 (1999).

[10]   R. M. Tiggelaar, A. W. Groenland, R. G. P. Sanders, and J. G. E. Gardeniers, J. Appl. Phys. **105**, 6 (2009).

[11]   W. T. Li, D. R. McKenzie, W. D. McFall, and Q. C. Zhang, Thin Solid Films **384**, 46 (2001).

[12]   J. D. Wu, J. Sun, X. X. Zhong, Z. Y. Zhou, C. Z. Wu, and F. M. Li, Thin Solid Films **350**, 101 (1999).

[13]   Y. Hirohata, N. Shimamoto, T. Hino, T. Yamashima, and K. Yabe, Thin Solid Films **253**, 425 (1994).

[14]   S. Sitbon, M. C. Hugon, B. Agius, F. Abel, J. L. Courant, and M. Puech, J. Vac. Sci. Technol., A **13**, 2900 (1995).

[15]   T. Aiyama, T. Fukunaga, K. Niihara, T. Hirai, and K. Suzuki, J. Non-Cryst. Solids **33**, 131 (1979).

[16]   M. Misawa, T. Fukunaga, K. Niihara, T. Hirai, and K. Suzuki, J. Non-Cryst. Solids **34**, 313 (1979).

[17]   T. Searle, *Properties of amorphous silicon and its alloys* (INSPEC, IEE, London, U.K., 1998).

[18]   A. Khan, J. Philip, and P. Hess, J. Appl. Phys. **95**, 1667 (2004).

[19]   M. M. Guraya, H. Ascolani, G. Zampieri, J. I. Cisneros, J. H. Dias da Silva, and M. P. Cantão, Phys. Rev. B **42**, 5677 (1990).

[20]   M. M. Guraya, H. Ascolani, G. Zampieri, J. H. Dias da Silva, M. P. Cantão, and J. I. Cisneros, Phys. Rev. B **49**, 13446 (1994).

[21]   W. L. Warren, J. Kanicki, J. Robertson, E. H. Poindexter, and P. J. McWhorter, J. Appl. Phys. **74**, 4034 (1993).

[22]   W. L. Warren, J. Robertson, and J. Kanicki, Appl. Phys. Lett. **63**, 2685 (1993).

[23]   R. Kärcher, L. Ley, and R. L. Johnson, Phys. Rev. B **30**, 1896 (1984).

[24]   A. Iqbal, W. B. Jackson, C. C. Tsai, J. W. Allen, and J. C. W. Bates, J. Appl. Phys. **61**, 2947 (1987).

[25]   A. J. Lowe, M. J. Powell, and S. R. Elliott, J. Appl. Phys. **59**, 1251 (1986).

[26]   A. Suhane, A. Arreghini, R. Degraeve, G. Van den bosch, L. Breuil, M. B. Zahid, M. Jurczak, K. De Meyer, and J. Van Houdt, IEEE Electron Device Lett. **31**, 77 (2010).

[27]   J. Robertson, Philos. Mag. B **63**, 47 (1991).

[28]   N. Umesaki, N. Hirosaki, and K. Hirao, J. Non-Cryst. Solids **150**, 120 (1992).

[29]   F. de Brito Mota, J. F. Justo, and A. Fazzio, Phys. Rev. B **58**, 8323 (1998).

[30]   P. Kroll, J. Non-Cryst. Solids **293**, 238 (2001).

[31]   P. Kroll, Mater. Res. Soc. Symp. Proc. **715**, 479 (2002).

[32]   P. Kroll, J. Eur. Ceram. Soc. **25**, 163 (2005).

[33]   S. Z. Karazhanov, P. Kroll, A. Holt, A. Bentzen, and A. Ulyashin, J. Appl. Phys. **106**, 053717 (2009).

[34] L. Giacomazzi and P. Umari, Phys. Rev. B **80**, 144201 (2009).
[35] K. Jarolimek, R. A. de Groot, G. A. de Wijs, and M. Zeman, Phys. Rev. B **82**, 205201 (2010).
[36] M. Ippolito and S. Meloni, Phys. Rev. B **83**, 165209 (2011).
[37] N. L. Anderson, R. P. Vedula, P. A. Schultz, R. M. Van Ginhoven, and A. Strachan, Phys. Rev. Lett. **106**, 206402 (2011).
[38] R. M. Van Ginhoven, H. Jónsson, and L. R. Corrales, Phys. Rev. B **71**, 024208 (2005).
[39] M. Benoit, S. Ispas, P. Jund, and R. Jullien, Eur. Phys. J. B **13**, 631 (2000).
[40] M. A. Szymanski, A. L. Shluger, and A. M. Stoneham, Phys. Rev. B **63**, 224207 (2001).
[41] S. H. Garofalini and W. Luo, J. Am. Ceram. Soc. **86**, 1741 (2003).
[42] X. T. Su and S. H. Garofalini, J. Appl. Phys. **97** (2005).
[43] S. Plimpton, J. Comput. Phys. **117**, 1 (1995).
[44] J. P. Perdew, K. Burke, and M. Ernzerhof, Phys. Rev. Lett. **77**, 3865 (1996).
[45] P. Giannozzi, et al., J. Phys.: Condens. Matter **21** (2009).
[46] J. P. Perdew and A. Zunger, Phys. Rev. B **23**, 5048 (1981).
[47] http://dft.sandia.gov/Quest/. The DFT simulations in this paper can be repeated online using the "nanoMATERIALS: SeqQuest-DFT" tool available in nanoHUB.org: https://nanohub.org/resources/3982, DOI: 10254/nanohub-r3982.1.
[48] A. Palaria, G. Klimeck, and A. Strachan, Phys. Rev. B **78**, 205315 (2008).
[49] Supplementary Material.
[50] X. Yuan and A. N. Cormack, Comput. Mater. Sci. **24**, 343 (2002).
[51] C. E. Jesurum, V. Pulim, and L. W. Hobbs, J. Nucl. Mater. **253**, 87 (1998).
[52] W. Y. Ching, L. Ouyang, and J. D. Gale, Phys. Rev. B **61**, 8696 (2000).
[53] I. Tomaszkiewicz, J. Therm. Anal. Calorim. **65**, 425 (2001).
[54] Y. Yokoyama, T. Nanba, I. Yasui, H. Kaya, T. Maeshima, and T. Isoda, J. Am. Ceram. Soc. **74**, 654 (1991).
[55] A. A. Mostofi, J. R. Yates, Y. S. Lee, I. Souza, D. Vanderbilt, and N. Marzari, Comput. Phys. Commun. **178**, 685 (2008).
[56] P. L. Silvestrelli, N. Marzari, D. Vanderbilt, and M. Parrinello, Solid State Commun. **107**, 7 (1998).
[57] J. Bauer, Phys. Status Solidi A **39**, 411 (1977).
[58] G. Onida, L. Reining, and A. Rubio, Rev. Mod. Phys. **74**, 601 (2002).
[59] P. A. Schultz, Phys. Rev. Lett. **96**, 246401 (2006).